

Microstructure Development in a New Generation S1300-Type Ultrahigh-Strength Structural Steel on Tempering

JANA, Buddhadev <<http://orcid.org/0000-0002-0690-9288>> and RANA, Radhakanta

Available from Sheffield Hallam University Research Archive (SHURA) at:

<https://shura.shu.ac.uk/35973/>

This document is the Published Version [VoR]

Citation:

JANA, Buddhadev and RANA, Radhakanta (2025). Microstructure Development in a New Generation S1300-Type Ultrahigh-Strength Structural Steel on Tempering. Steel Research International: 2401072. [Article]

Copyright and re-use policy

See <http://shura.shu.ac.uk/information.html>

Microstructure Development in a New Generation S1300-Type Ultrahigh-Strength Structural Steel on Tempering

Buddhadev Jana* and Radhakanta Rana*

Product development routes for new generation ultrahigh-strength structural steels such as S1300 are currently not well-defined, warranting studies on their alloy design, processing, and microstructure–property correlations. This study aims to bridge the gap in understanding of these aspects by investigating a boron-treated, low-carbon, S1300-type alloy steel produced via the direct-quench and tempering (DQ&T) route. The study includes detailed characterization of microstructure development under widely varied tempering temperatures using scanning electron microscopy (SEM), electron backscatter diffraction (EBSD), X-ray diffraction (XRD), dilatometry, and hardness measurements. It reveals three tempering stages of martensite, based on changes in hardness and corroborated by full width at half maximum (FWHM), microstrain, crystallite size, and lattice distortion of martensite. A strong linear correlation between hardness and FWHM is found. The microstructure remained predominantly martensitic (BCT) from its DQ to all tempered states up to 700 °C. Furthermore, EBSD analysis reveals the presence of bainite alongside tempered martensite. Nucleation of fine η -Fe₂C, formation and growth of Fe₃C and other alloy carbides, and secondary hardening are responsible for the three distinct stages of tempering. Finally, a new parameter named “microstrain-crystallite size parameter” is proposed to establish an empirical relationship for predicting hardness changes during tempering of S1300-type steels.

characteristic values of ultrahigh yield strength (YS), typically over 1300 MPa. These steels provide a high strength-to-weight ratio, resulting in significant weight savings for heavy load-bearing structures. There is a growing demand for UHSS in the lifting and excavating market, particularly for applications such as heavy cranes.

The development of structural steel grades has evolved over the years. It began with the development of S355 grade around 8 decades ago, which had a minimum YS of 355 MPa.^[1–3] Since then, several grades have been developed, including S420, S460, S500, S550, S690, S700, and so on. These lower YS structural grades are used for variety of applications including in automotive, lifting and excavating, line pipe, and pressure vessel.^[4–6] These grades are typically microalloyed and processed through normalizing (N), thermomechanical processing (TMP), etc. For higher YS structural steel grades such as S900, S960, S1100, S1300, a quench and tempering (Q&T) route is often applicable where the steels are first cooled rapidly below the martensite start

temperature (M_s) to achieve the ultrahigh strength and then subsequently tempered to improve the toughness and ductility related material properties.

S1300 is the newest addition to the structural steel grades and has been under development for more than a decade by several steel producers in Europe and America.^[1] However, there is a significant knowledge gap regarding the development of the grade, particularly with alloy design, process optimization, and microstructure/property correlation.

Steel producers are continuously searching for cost-effective and efficient methods to remain competitive. The European Union's green initiatives have introduced stricter regulations, compelling the industry to discover innovative solutions for reducing greenhouse gas emissions. Enhancing process efficiency is essential for sustainability. As the production route for the new generation grade S1300 is still not well established, efforts are concentrated on optimizing its alloying strategy and processes.


In the literature, there are virtually no studies on the aspect of alloy design and processing route and microstructure–property relations for S1300 steels. However, only a few studies on the weldability of S1300 are available.^[1,7] These focused mainly on

1. Introduction

The structural steel grade, S1300, represents a new generation of ultrahigh-strength steel (UHSS) defined by minimum

B. Jana
School of Engineering and Built Environment
Sheffield Hallam University
Sheaf Building, City Campus, Howard Street, Sheffield S1 1WB, UK
E-mail: b.jana@shu.ac.uk

R. Rana
Tata Steel
Wenckebachstraat 1, 1970 CA IJmuiden, The Netherlands
E-mail: radhakanta.rana@tatasteeleurope.com

 The ORCID identification number(s) for the author(s) of this article can be found under <https://doi.org/10.1002/srin.202401072>.

© 2025 The Author(s). Steel Research International published by Wiley-VCH GmbH. This is an open access article under the terms of the Creative Commons Attribution License, which permits use, distribution and reproduction in any medium, provided the original work is properly cited.

DOI: 10.1002/srin.202401072

microstructure–property relations for welded structures generated using various welding methods. However, these studies, although providing some clues on how microstructure changes under high-temperature welding conditions, are not sufficient to understand microstructural changes related to steel production routes, which include processes such as hot rolling, direct quenching (DQ), and tempering. This understanding is pivotal for the successful, cost-effective development of the S1300 grade.

However, a wide range of studies exists on UHSS, with a minimum YS of 1300 MPa, for applications such as automotive, and aerospace,^[8–16] but with microstructure and alloy strategies which are very different from S1300 structural grade for lifting and excavating sector. These UHSS from automotive and aerospace sectors are reported using high silicon, high manganese alloy philosophies to obtain bainitic, transformation-induced plasticity (TRIP) type or quenching and partitioning (Q&P) type steels. These grades, although promises YS significantly higher than 1300 MPa, are relatively more expensive and very difficult to process compared to S1300 structural steel developed via martensite matrix-based lean alloy philosophy. For example, high manganese steels show high hot strength^[17] and are prone to cracking during casting process, and high Si steels are difficult to descale before hot rolling due to the formation of sticky oxide scale.^[12] Furthermore, the required levels of Mn and Si in these steels increase the hot rolling force tremendously limiting the rolling capacity. Moreover, application of the required thermal cycles for obtaining high amounts of retained austenite (RA) in these steels is very difficult to achieve on an industrial scale. Therefore, the martensite-based S1300 structural steels is the foremost favored candidate for achieving such high levels of YS.

This study investigated how DQ and tempering heat treatment affect the microstructure and hardness of an ultrahigh-strength S1300-like steel. Understanding these changes is essential for achieving an excellent combination of strength and ductility and cost-effective development of S1300 grade. The study also explored relevant crystallographic parameters that strongly influence the hardness of the steel and developed new empirical relations with hardness that are useful for future S1300 development.

2. Experimental Section

2.1. Material

An ultrahigh-strength S1300 type steel was studied. Sections of the steel, in its hot rolled and direct quenched (DQ) state, were received from Tata Steel Netherlands with the composition as shown in Table 1. The previous treatment history of the steel included casting in pilot-scale, homogenization of the ingots at 1230 °C for 1 h, rough rolling to a transfer gauge of 38 mm, reheating at 1230 °C for 1 h, and then hot rolling to a nominal gauge of 6 mm in 6 passes. The hot rolling was completed with

a finish rolling temperature of around 900 °C, and then the strips were water quenched in a run-out table (ROT) to room temperature with a cooling rate $\approx 20\text{ °C s}^{-1}$.

2.2. Tempering Treatments

The as-received hot rolled DQ steel was cut into $20 \times 20 \times 6$ mm specimens, and these samples were tempered isothermally for 2 h in a very wide temperature range from 200 to 700 °C at each 50 °C interval under argon atmosphere using an ELITE programmable induction tube furnace. The samples were heated at 5 °C min^{-1} until they reached the tempering temperature, held for 2 h, and then were removed from the furnace and allowed to cool to room temperature in air. As presented later in Section 3.1, the steel when tempered for 7 h at 250 °C achieved the maximum YS, but still it fell slightly short of the YS level of 1300 MPa. Therefore, for this study the tempering time was shortened to 2 h.

2.3. Hardness Measurements

The Vickers hardness of the tempered specimens was measured using a Wilson Automatic Vickers Hardness tester under a 10 kgf force. Hardness was measured along the center line on the thickness plane in the rolling direction of the specimens, after metallographically polishing the surface to the mirror finish which ensured complete elimination of any surface scale that could affect the hardness values. The 10 kgf force was chosen for its high repeatability after conducting a series of hardness tests under forces ranging from 5 kgf to 50 kgf in 5 kgf intervals. A minimum of 10 measurements were made for each heat treatment condition to determine the average hardness values reported here.

2.4. Dilatometry

Dilatometric experiments, using Bähr DIL805 dilatometer, were conducted to determine the transformation behavior of the steel under different cooling rates. Flat-shaped dilatometry specimens measuring $10 \times 5 \times 6$ mm were austenitized at 900 °C for 5 min using a heating rate of 10 °C s^{-1} , followed by cooling to room temperature with the cooling rates of 10, 20, 55, 120, and 310 °C s^{-1} by use of argon (for 10 and 20 °C s^{-1}) or helium (for 55 °C s^{-1} or faster). The specimen holder was made of Si_3N_4 and Type S thermocouple (Pt-10%Rh) was used for temperature measurement, spot-welding it in the middle of the specimen surface, on the 10×5 mm area.

2.5. X-Ray Diffraction (XRD)

XRD measurements were conducted to estimate the evolution of lattice parameter and lattice strain of martensite, as well as any RA content in the samples, at the tempering temperatures

Table 1. Steel composition in wt%. CEV = carbon equivalent value as per the formula of American Welding Society (AWS).

C	Mn	Cr	Mo	Nb	Ti	V	B	Si	Al	S	P	Fe	CEV
0.22	1.02	0.39	0.56	0.04	0.016	0.10	0.0025	0.016	0.043	0.0018	0.013	Balance	0.60

studied. XRD sample preparation included polishing the specimens to about 1.5 mm and then etching for 15 min using a chemical solution containing 580 mL of H_3PO_4 , 330 mL of H_2O_2 , 8 mL of ethylene glycol, and 80 mL of demineralized water.

XRD patterns were recorded in the 2θ range (the angle between the incident and the diffracted beams) of 30 to 165° in a Panalytical Xpert PRO standard powder diffractometer using $\text{Co-K}\alpha$ radiation with a step size of $0.026^\circ/\text{s}$. The changes in the lattice parameter (c/a ratio or a/c ratio) with tempering temperature in the specimens were analyzed by the Topas (version 5) software package. For this purpose, first the software was used to fit the lattice constants (a and c) of all recorded XRD patterns using a Le Bail fit (i.e., a pattern decomposition). In pattern decomposition, the availability of full crystal data is not required. This is possible because the reflections or peak intensities are obtained directly from an iterative partitioning of the experimental intensities (recorded XRD pattern) according to the intensities calculated from the model function. To enable this, an HKL phase (space group I4mm, tetragonal) was created in which the lattice constants a and c were allowed to vary between 0.283 – 0.287 nm and 0.287 – 0.307 nm respectively. To accommodate for crystallite size and strain effects, crystallite size and strain were allowed to refine between 45 – 500 nm and 0.01 – 1 respectively. For the background, a Chebyshev Polynomial of 5th order as well as the $1/X$ Bkg function was selected. The standard deviation of a and c values were in the range of 0.001 – 0.002% and 0.002 – 0.006% respectively.

The full width at half maxima (FWHM) of the XRD peaks was analyzed for the estimation of lattice strain. The FWHM was determined by analyzing the XRD patterns with the OriginPro24 software. The details of this analysis are described directly later in Section 3.3.

2.6. Scanning Electron Microscopy (SEM)

Microstructure on the longitudinal thickness plane (plane of rolling direction and normal direction, i.e., RD-ND plane) along the rolling direction was examined using a Quanta 650 scanning electron microscope (FEI corporation, The Netherlands). Metallographic specimen preparation involved mounting in conductive bakelite, mechanical polishing to a mirror finish, and etching with 2% nital solution.

The analysis of carbides was done on selected samples. Measurements were performed on the RD-ND plane using a Zeiss Ultra55+ microscope with a secondary electron (SE) inLens detector. Samples were polished and then etched with Picral solution to highlight C-rich areas (carbides), and then images were taken from the mid-thickness of the RD-ND plane. The analysis was done based on 5 images with an area of $5.12 \times 3.84 \mu\text{m}^2$ with 5 nm pixel size, which amounts to $98 \mu\text{m}^2$ area in total.

2.7. Electron Backscatter Diffraction (EBSD)

The EBSD measurements were done on the RD-ND plane of the same selected samples as for the carbide analysis. The measurements were performed with Zeiss FEG-SEM Ultra55+ equipped

with Oxford Instruments EBSD Symmetry S3 detector with software Aztec version 6.1. Samples were polished with the last step with colloidal silica. The SEM settings used for the measurements were 15 kV voltage and $120 \mu\text{m}$ aperture (≈ 8 nA). Areas of $200 \times 150 \mu\text{m}^2$ with step size of 75 nm were measured at mid thickness. The collected Kikuchi patterns were first analyzed with Hough transform method. Afterwards, pattern matching was used to improve indexing and angular resolution of the datasets using MapSweeper in the software AztecCrystal version 3.2. The maps of geometrically necessary dislocations (GND) were calculated using Burgers vector $0.5a \langle 110 \rangle$ (a being the lattice parameter).

3. Results

3.1. Hardness and Tensile Properties

Figure 1 shows hardness as a function of tempering temperature of the steel studied. The tempering temperature of 20°C corresponds to the as-received steel, which is in its hot rolled DQ state. As evident in Figure 1, the hardness that can be achieved for the studied steel from its DQ state to tempering state at 700°C ranges from 497 to 376 HV10.

As evident in Figure 1, the hardness did not decrease linearly with the tempering temperature; instead, it followed three distinct stages of change as indicated by “Tempering Stage 1 to 3” in Figure 1. The tempering stage 1 ranges up to the tempering temperature of 200°C , where the effect of tempering on hardness was minimal, showing around 3% decrease in hardness from its DQ state to tempering at 200°C . However, a pronounced effect of tempering on the hardness was found in tempering stage 2, which ranges from over 200°C to 500°C , showing a hardness fall of 20%. The tempering stage 3 ranges from over 500°C to 700°C , where secondary hardening followed by further softening of the steel was observed.

The trend depicted in Figure 1 broadly aligns with the published data for ultrahigh-strength steels.^[18] However, it is crucial to accurately assess the variation in hardness with tempering temperature for the S1300 type steel studied and to have a detailed understanding of the underlying mechanisms for the

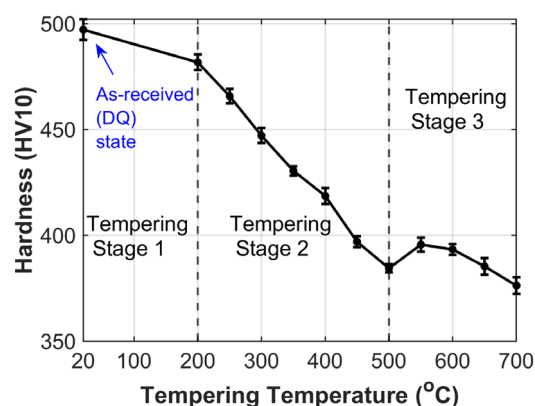


Figure 1. Hardness vs. tempering temperature plot of the investigated steel.

observed trend, which has not been thoroughly studied before. This understanding is essential for establishing a successful product development route for a S1300 product.

The tensile properties of the steel were measured in its DQ state as well as at various tempering temperatures after a tempering duration of 7 h, which was preferred for industrial production of the grade. The engineering stress-strain curves and the corresponding property values are presented in **Figure 2**. The maximum YS achieved after 7 h of tempering was at 250 °C, which fell slightly short of the minimum YS requirement for S1300 steel. Therefore, the current study was undertaken with a shorter tempering time of 2 h. However, it should be mentioned that although the current study used a 2 h tempering duration, it did not verify tensile properties for this period. Instead, it focused on gaining a detailed understanding of microstructural changes and various other crystallographic parameters at closely spaced tempering temperatures for the 2 h tempering duration.

As shown in **Figure 2**, the measured YS values display a trend similar to that of the hardness presented in **Figure 1**. Although the tempering time in **Figure 2** was 7 h, compared to 2 h in **Figure 1**, the three stages of the tempering effect are clearly observable in **Figure 2**. However, it is important to note that the transition temperatures for these three stages may vary with tempering time. For instance, in **Figure 2**, the tempering at 250 °C falls within tempering stage 1, whereas in **Figure 1**, the stage 1 was limited to 200 °C. It should also be noted that in tempering stage 1, the YS of the steel increases from DQ state to 250 °C tempering state, whereas the ultimate tensile strength (UTS) decreases. Then, in the tempering stage 2, both the YS and UTS decrease up to tempering at 500 °C before increasing again in tempering stage 3 due to secondary hardening. The increase in the YS in tempering stage 1 can be attributed to the relaxation of internal stresses at the low temperature tempering as shown by Hutchinson et al.,^[19] and the decrease in UTS is due to the loss of tetragonality of the BCT martensitic matrix as will be observed later from the XRD results.

3.2. Martensite Start Temperature (M_s)

Determining the martensite start temperature (M_s) is essential for the microstructural characterization of the studied steel, which is presented later. **Figure 3a** presents the dilatometric curves for the cooling path for the steel specimens subjected to a wide range of cooling rates following austenitization at 900 °C: from 10 to 310 °C s⁻¹.

The M_s values for each cooling rate were determined using the tangent method,^[20] and these M_s values are plotted in **Figure 3b** against the cooling rate. The M_s is, as expected, dependent on the cooling rate.^[21] Initially, with the increase in cooling rate from 10 to 20 °C s⁻¹, the M_s decreased, and then it increased with further increase in cooling rate. With slow cooling rates, some carbide precipitation may occur, which will deplete carbon from austenite raising the M_s . The M_s will decrease with faster cooling rate when carbide precipitation will be lesser resulting in more carbon enrichment in austenite.^[21] However, the increase in M_s , after a drop, with further increase in cooling rate is interesting and can possibly be due to the introduction of internal stresses in the material arising from fast quenching as observed by Liu et al. in martensitic stainless steel.^[22] It should be noted that the S1300-type steel investigated here was quenched at a rate of ≈ 20 °C s⁻¹ (Section 2.1), up to which a decrease of M_s was observed with increasing cooling rate.

3.3. XRD Analysis

Figure 4 shows XRD patterns of the steel in DQ and various tempered conditions. The XRD analysis was conducted to check whether the steel contained any RA, as previous studies on a wide range of UHSS grades reported the presence of RA.^[13,23,24] However, in this study, no RA was found in the samples for all the heat treatment conditions studied, as evidenced by the absence of any peak corresponding to FCC crystal structure. The peaks in **Figure 4** correspond to the BCC structure,

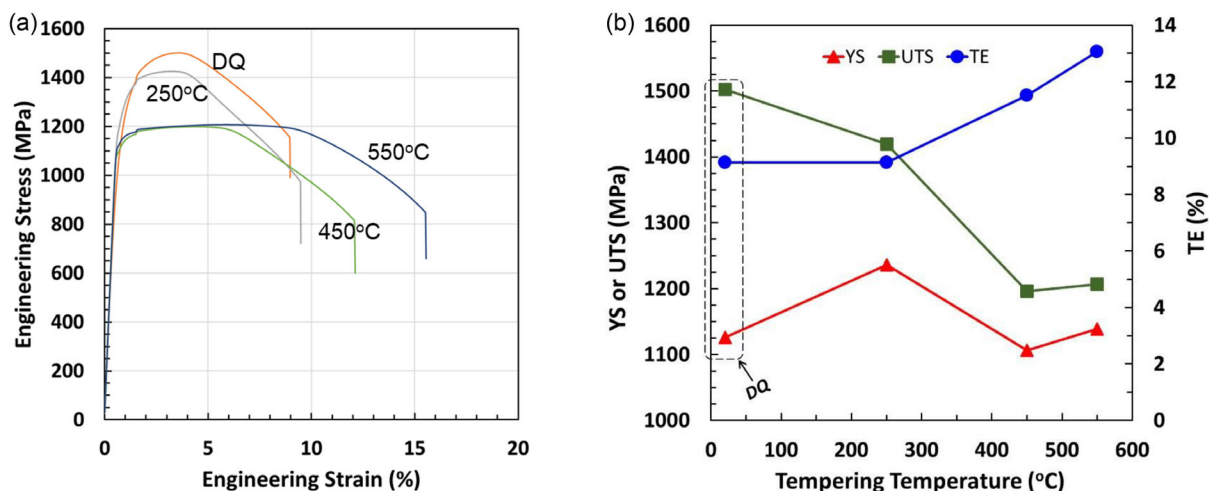


Figure 2. Tensile behavior of the steel directly quenched (DQ) and tempered at different temperatures for 7 h: a) engineering stress-strain curves and b) YS, UTS, and total elongation (TE) plotted against tempering temperature. Tensile tests were done using so-called Euronorm A50 specimens (as per EN10002-1 with 50 mm gauge length and 12.5 mm gauge width).

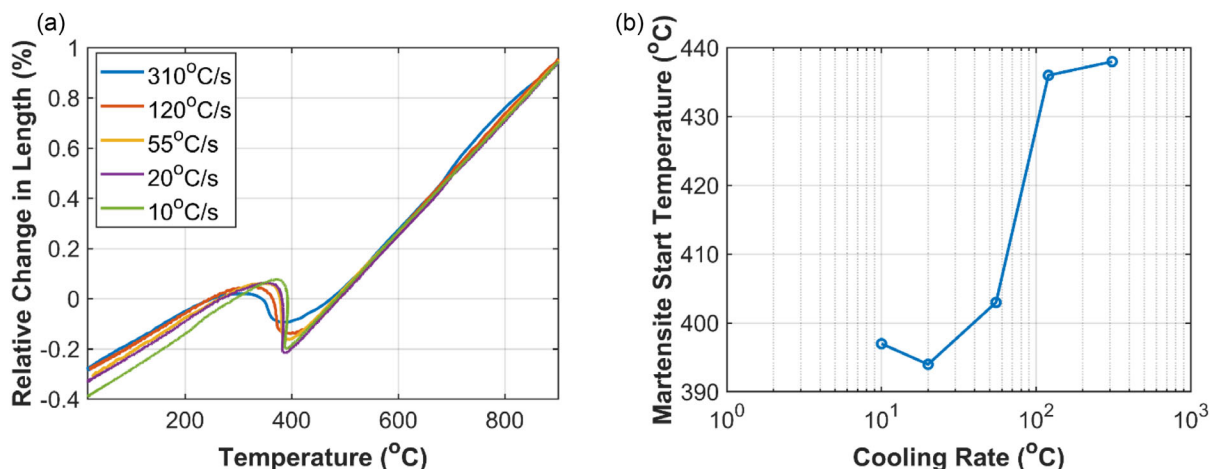


Figure 3. Dilatometry results of the steel specimens under various cooling rates following austenitization—a) full cooling path and b) plot of M_s against cooling rate.

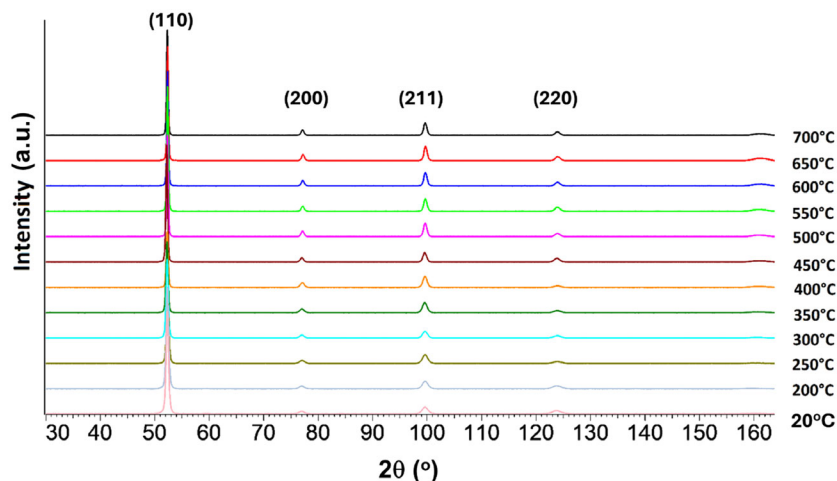


Figure 4. XRD patterns of the steel in DQ and tempered conditions showing BCC peaks. No FCC peak for austenite was present.

suggesting they originated from the martensite phase present in the steel.

Figure 5 shows the effects of tempering temperature on the tetragonality of martensite lattice parameter (c/a and a/c ratio) of the steel determined from XRD data. The c/a ratio was greater than one in both DQ (corresponding to 20 °C) and in all the tempered conditions (ranging from 200 °C to 700 °C). The graph also depicts the inverse values of c/a (as a/c ratios), which were less than one in all examined heat treatment conditions. This suggests that the microstructure of the steel was BCT martensitic under all the heat treatment conditions. This is contrary to the common observations that during tempering, martensite transforms into BCC ferrite and cementite,^[25] especially at higher tempering temperatures. The SEM microstructures shown in the following sections also provide evidence of martensitic lath microstructure. Figure 5 shows the largest change in the c/a ratio (or a/c ratio) occurring from 200 to 450 °C, with

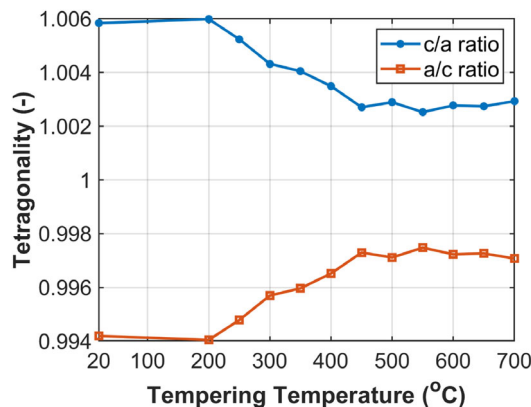


Figure 5. Change in tetragonality ratio of martensite in the steel against tempering temperature.

a plateau reached after 450 °C. These changes will be discussed further in the following sections in the context of the microstructural changes observed in this study.

Figure 6 shows the effect of tempering temperature on the full width at half maximum (FWHM) determined using the Voigt peak function fitting method on the XRD peaks of martensite shown in Figure 4. For estimation of FWHM, first, the recorded XRD pattern of a particular treatment condition was sectioned into four 2θ regimes: 45–60°, 70–90°, 90–110°, and 115–135°. Then, the OriginPro24 software package was used to fit the peaks with a least square (R^2) value of > 99.5%. The Voigt peak fitting method demonstrated the lowest error compared to the other peak fitting methods evaluated in this study. A comparison of the errors associated with the different peak fitting methods can be found in **Appendix 1**.

In Figure 6, it is evident that the FWHM value is more pronounced at higher 2θ angles. The FWHM values provide a semi-quantitative indication of crystallite sizes and microstrains resulting from the introduction of dislocations, stacking faults, and so on.^[26] It is also evident from Figure 6 that the change in FWHM values was minimal up to 200 °C, then decreased significantly with increasing tempering temperatures up to 500 °C, and then finally plateaued up to 700 °C.

From the FWHM values in Figure 6, the corresponding microstrain and crystallite size values were calculated based on the Williamson–Hall procedure^[27,28] and are presented in **Figure 7**. In calculating the microstrain and crystallite size values, the following equation was used.

$$\beta^2 \cos^2 \theta = \left(\frac{\lambda}{L} \right)^2 + 16 \epsilon^2 \sin^2 \theta \quad (1)$$

where λ is the wavelength (for Co-K α radiation, in nm), β is FWHM (in radians), L is crystallite size (in nm), ϵ is microstrain (in %), and θ is diffraction angle (in radians).

Using the FWHM data presented in Figure 6, $\beta^2 \cos^2 \theta$ was plotted against $16 \sin^2 \theta$, and the gradient and y-intersect of the best-fit line were calculated. These values were appropriately used in Equation (1) to calculate the microstrain and crystallite size values, as shown in Figure 7.

Figure 7 shows that the microstrain varies with tempering temperature, similar to that observed for FWHM in Figure 6.

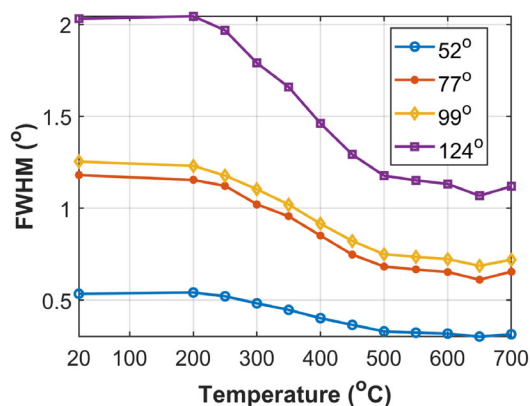


Figure 6. Effect of tempering temperature on FWHM of martensite generated using Voigt profile fit to the XRD peaks.

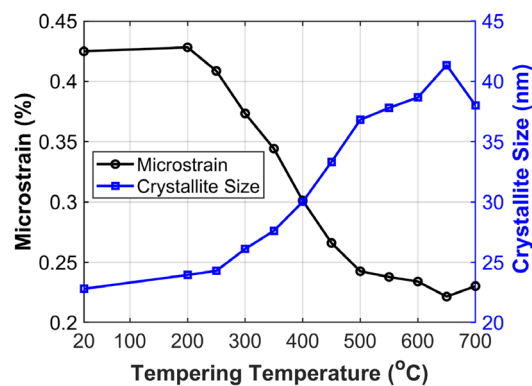


Figure 7. Calculated microstrain and crystallite size calculated from the FWHM data in Figure 6, based on the Williamson–Hall procedure.^[15,17]

The crystallite size was found to increase with tempering temperature. These are further discussed later in this article.

3.4. SEM Micrographs

3.4.1. DQ

Figure 8 shows SEM SE micrographs for the DQ condition of the steel. The micrographs revealed martensite laths consisting of blocks of (parallel and nonparallel) laths aggregated as packets within a prior austenite grain.^[18,29] The martensite laths (arrow B) were extremely fine, with a thickness of $\approx 0.2 \mu\text{m}$. Such fine martensite laths are expected to be more reactive during tempering treatment due to the presence of very large lath interface areas;^[18] this aspect is relevant to the tempered microstructures, which will be analyzed in the subsequent sections.

Under DQ condition, the M_s of the steel is expected to be around 405 °C, as the cooling rate in DQ operation was around 20°C s^{-1} (Section 2.1), as shown in Figure 2. Under such quenching conditions, the steel, with such a lower carbon content and high M_s , is expected to undergo autotempering to some extent. Autotempering occurs due to the high mobility of supersaturated carbon in martensite crystals during cooling from high M_s , leading to its segregation to inter-lath boundaries and dislocations. The carbon segregation is more effective, especially under the relatively slower quenching conditions experienced during DQ operation. In addition, plate-like cementite can also be found in the autotempered regions.^[18] These autotempered martensite regions (arrow A) are also visible in Figure 8b.

RA was not present in the steel in its quenched (DQ) or tempered conditions, as evident by the XRD analysis shown in Figure 4. Therefore, RA was not present in the microstructures in Figure 8, albeit the microstructure contains brighter inter-lath boundaries, which many previously published studies have reported as RA for their steels with similar compositions.^[23,24] However, in present steel, these were not RA but appeared due to different exposures of the inter-lath boundary in contrast to the main body of the lath.

As revealed by dilatometry in Figure 3, S1300 underwent only an austenite-to-martensite transformation under DQ condition. Given that the steel does not have any RA, the microstructure in

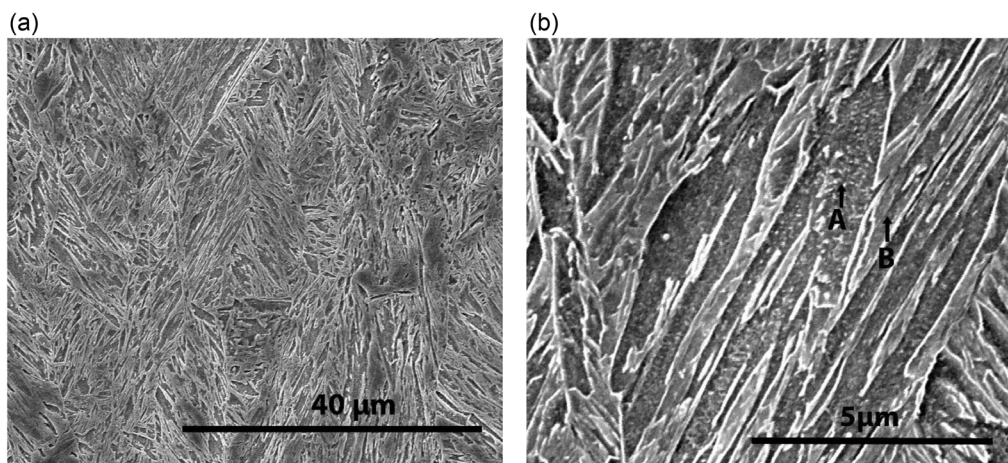


Figure 8. SEM micrograph of the steel after DQ at a) low (3000X) and b) high (20,000X) magnifications, showing laths of martensite and some autotempered areas.

Figure 8 is martensitic, consisting of fresh martensite (arrow B) and autotempered martensite (arrow A).

3.4.2. Tempering Stage 1

This tempering stage of martensite is sometimes referred to by various other studies as low-temperature tempering (LTT), and it ranges from 150 °C to 200 °C.^[18] The SEM micrographs of the steel after tempering at 200 °C are shown in **Figure 9**, which, when compared with its DQ micrographs shown in **Figure 8**, shows the following microstructural constituents: (1) martensite laths, (2) tempered martensite regions, and (3) very fine precipitates throughout the microstructures.

In **Figure 9**, the microstructure predominantly consisted of lath martensite, with areas of tempered martensite regions resembling the autotempered regions identified in the DQ micrographs in **Figure 8**. Both the laths and tempered areas were found to be relatively coarser than in the DQ steel. In addition, the dominant change in these microstructures was the widespread presence of very fine precipitates, which could not be analyzed using

SEM-EDX techniques. Various earlier studies have reported the presence of such fine precipitates during LTT of various low- and medium-carbon HSLA steel. These are reported as eta (η) transitional carbides of iron or η -Fe₂C of orthorhombic crystal structure.^[18,30,31] These η -Fe₂C carbides are previously reported to have a plate-like shape with a thickness range of 3–5 nm and precipitate in an interval of about 10 nm mainly on the dislocation and inter-lath boundaries.^[26,32] These transitional carbides are reported to strengthen steel by the dislocation pinning method and are also reported to increase hardness, YS and UTS in some steels from their quenched state.^[18,33] In this study, the hardness of the studied steel was found to be marginally reduced after tempering at 200 °C, although the YS increased (**Figure 1 and 2**).

3.4.3. Tempering Stage 2

This tempering stage of martensite is also referred to by various other studies as intermediate temperature tempering (ITT).^[18] During this stage, hardness decreases drastically as the tempering temperature increases. Typical microstructural changes

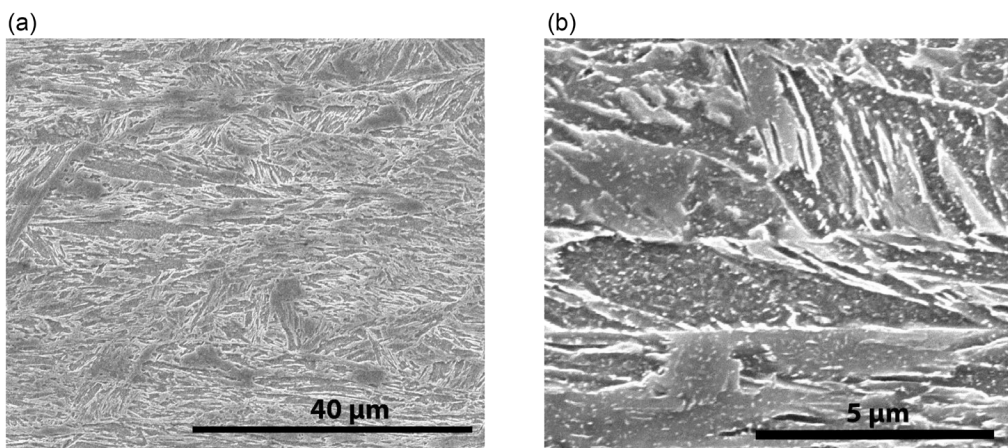


Figure 9. SEM micrographs of the steel after tempering at 200 °C at a) low (3000X) and b) high (20,000X) magnifications.

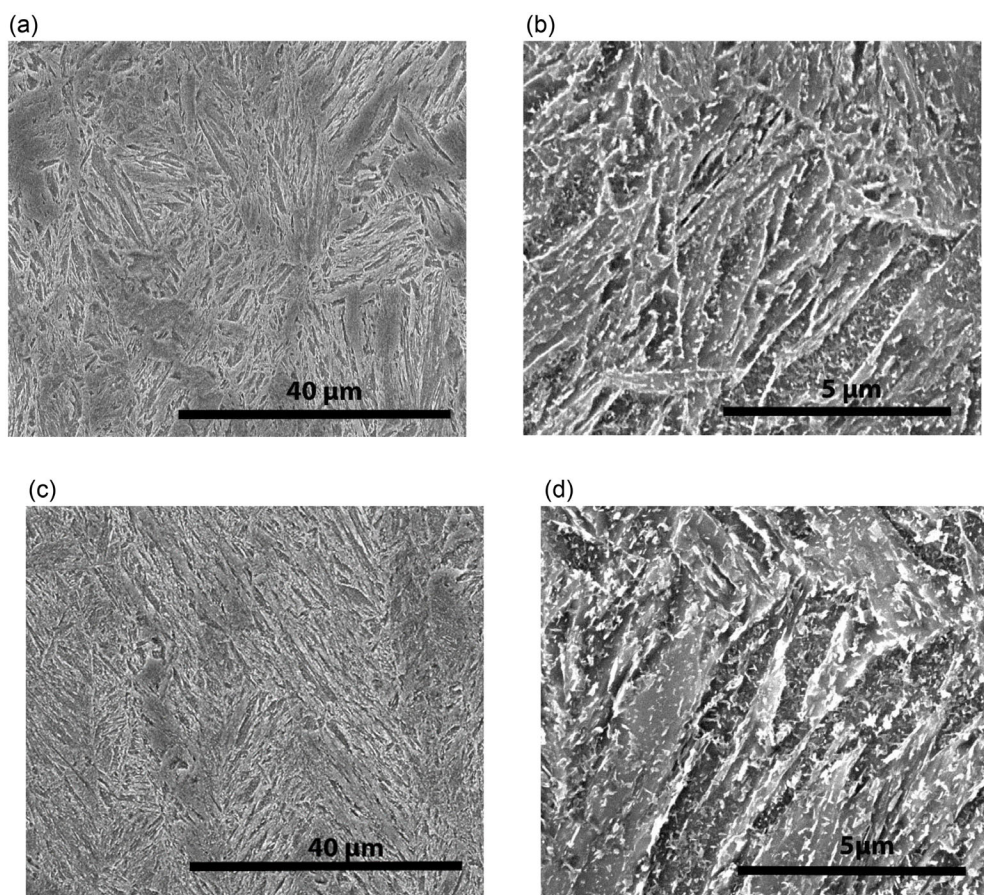


Figure 10. SEM micrographs of the steel after tempering at 250 and 350 °C at low (3000X) and high (20,000X) magnifications: a) 250 °C, low magnification, b) 250 °C, high magnification, c) 350 °C, low magnification, and d) 350 °C, high magnification.

within stage 2 are depicted in **Figure 10** and **11**. These changes mainly included the precipitation of iron carbide and the coarsening of martensite lath and tempered regions.

Martensite lath coarsening became more noticeable as the tempering temperature increased (see **Figure 10** and **11**). This was expected because of the elimination of low-angle grain boundaries at higher tempering temperatures.^[18,34] The lath coarsening contributed significantly to the substantial reduction in hardness observed during this tempering stage, along with several other factors responsible for the hardness change, which will be discussed later in this article.

The most significant microstructural change during stage 2 was the abundance of precipitates, which increased in size with temperature. The large precipitates were detected as iron carbide (Fe_3C) after tempering at 500 °C, as shown in **Figure 11c**. Previous studies on low- and medium-carbon quenched and tempered steels identified these precipitates as plate-shaped iron carbide (Fe_3C). These precipitates form as a result of the transformation of transitional eta iron-carbides ($\eta\text{-Fe}_2\text{C}$) into Fe_3C . Furthermore, it is well known that any RA present in the microstructure also undergoes a transformation into Fe_3C .^[18,30] However, the steel investigated here did not contain any RA; therefore, this is not applicable.

These precipitates are expected to consist of Fe_3C , which towards the higher temperature of tempering stage 2, may coexist with carbides or carbo-nitrides of other alloying elements, such as Mn, Cr, and Mo, present in the composition of the steel.^[18] The presence of M_6C carbides and MX carbonitrides of various carbide-forming elements has been previously observed in the microstructures of high-strength steels tempered at temperatures similar to stage 2.^[33]

Close scrutiny of the **Figure 10, 11** reveals precipitate growth with tempering temperature, which is expected to be incoherent and less effective in pinning dislocation movement. The precipitate growth was also a factor for the significant hardness reduction observed in tempering stage 2 (**Figure 1**).

3.4.4. Tempering Stage 3

In the literature, this tempering stage is sometimes also termed as high-temperature tempering (HTT).^[18] Typical SEM micrographs of the steel under tempering stage 3 are shown in **Figure 12** and **13**, which broadly reveal further coarsening of martensite grains and precipitates as the tempering temperature is increased. In addition, some microstructural changes related

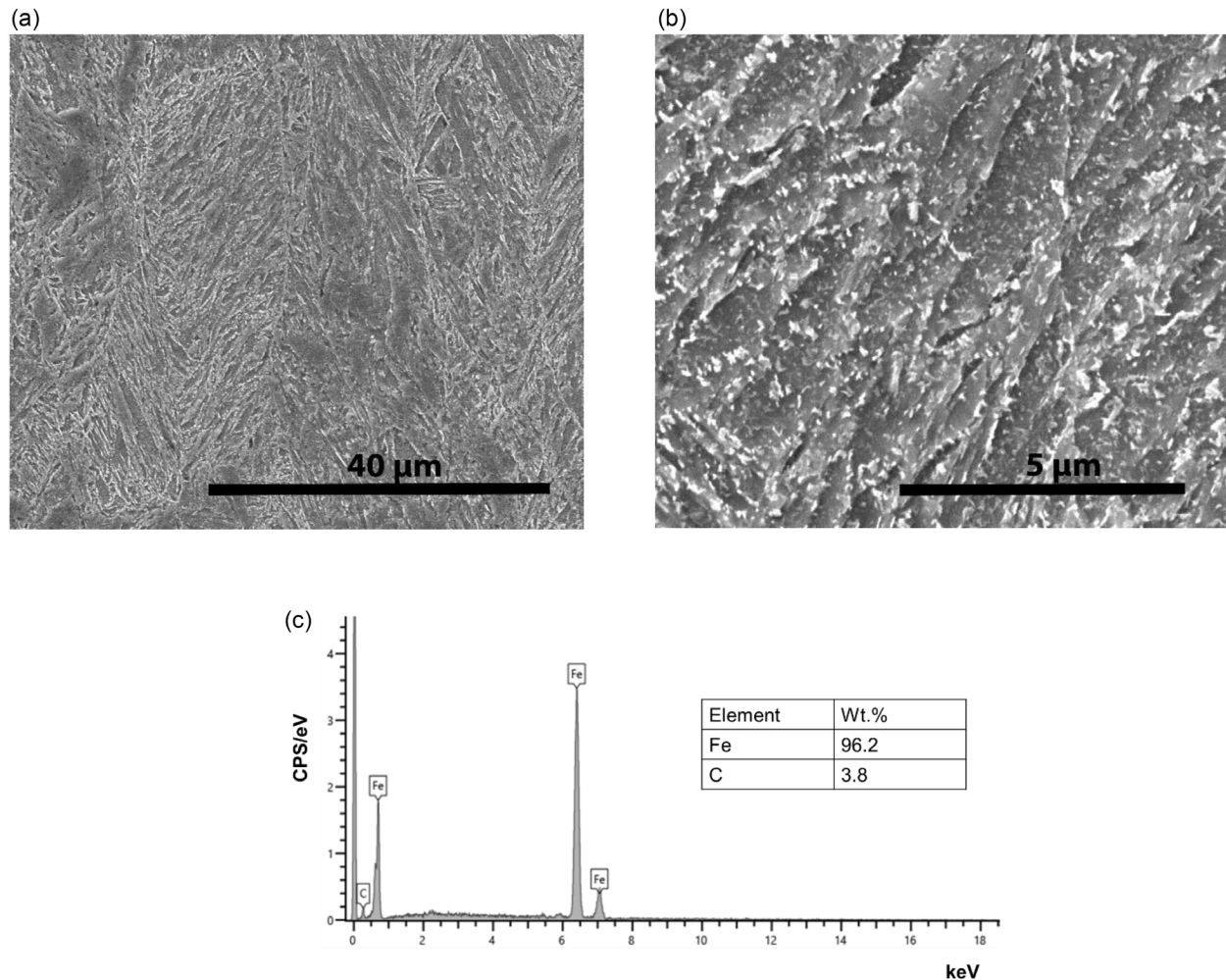


Figure 11. SEM micrographs of the steel after tempering at 500 °C at a) low (3000X) b) high (20,000X) magnifications, and c) EDX spectra of the precipitates.

to the secondary hardening are observed, especially after tempering at 550 °C, Figure 1, 12a,b.

It is interesting to note that lath martensite structure, with elongated and parallel morphology, remained present even after tempering at temperatures as high as 700 °C. The coarsening of martensite crystals with an increase in tempering temperature, in **Figure 13–15**, was expected, as the elimination of low-angle grain boundaries between small grains and movement of grain boundary has been previously reported to be operative during tempering of high-strength steel at similar conditions.^[18,34]

The precipitates in **Figure 12** and **13** were of varied sizes (shown using arrow A for finer and B for larger precipitates on the SEM images of the specimens tempered at 550 °C). The finer precipitates were responsible for secondary hardening observed at the 550 °C tempering state and, to some extent, at the 600 °C state, see **Figure 12**. When compared with the micrograph for 500 °C tempered specimens in **Figure 11**, these fine precipitates in **Figure 12a,b** were newly formed, especially visible in the intralath regions. These are expected to be the carbide and carbonitride of elements such as Cr, Mo, and V, present in the steel

composition and are well known to provide secondary hardening in steel.^[13] Evidence for the presence of these elements was found when some of the larger precipitates were analyzed using SEM-EDX, see **Figure 13**.

The larger precipitates in **Figure 12, 13** are the result of further coarsening of iron-carbide and carbide/carbonitrides of another element that formed during tempering stages 1 and 2, including the fine precipitates responsible for secondary hardening at the lower temperatures of tempering stage 3. EDX analysis for some of these larger precipitates in **Figure 13c** revealed the presence of Mn and Cr in them. Some previous studies have reported the presence of Cr_7C_3 in the quenched and tempered microstructure of high-strength steels, especially when tempered at 650 °C.^[34] The presence of carbide and carbonitrides of Mo, in the form M_6X , in the microstructure of high-strength steels was also reported previously.^[33]

Based on the above literature evidence, the larger precipitates in the present steel are expected to be iron-carbide coexisting with carbides and carbonitride of other elements, such as Mn, Mo, Cr, and V, which are also present in the current steel composition, see **Table 1**.

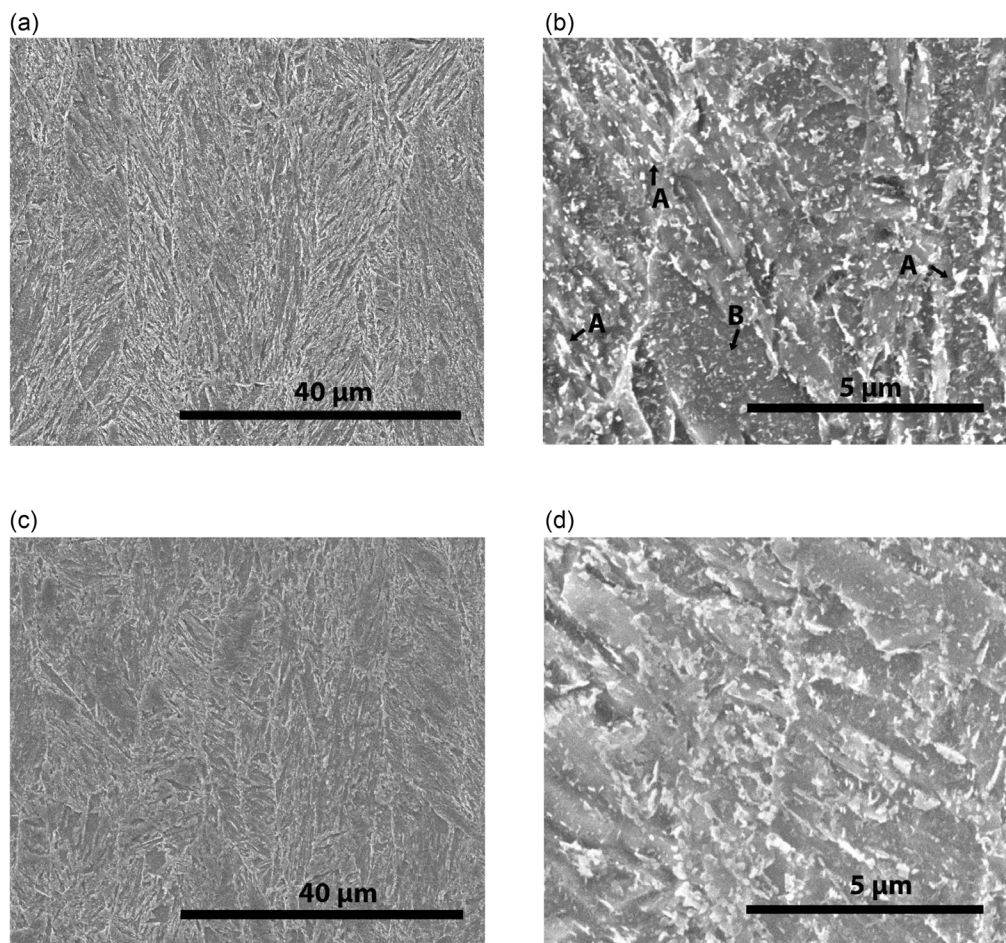


Figure 12. SEM micrographs of specimens tempered at 550 °C and 600 °C at low (3000X) and high (20,000X) magnifications: a) 550 °C, low magnification, b) 550 °C, high magnification, c) 600 °C, low magnification, and d) 600 °C, high magnification.

3.5. Carbide Analysis Using SEM

Figure 14 shows the distribution of carbides in various heat treatment conditions. The size, aspect ratio, and density of the carbides under each heat treatment condition are presented in Figure 15. These results are in line with the SEM micrographs presented in Section 3.4. Under DQ conditions, carbides are evident in both grain boundary and intralath locations, revealing that the martensite was autotempered, due to the reasons described in Section 3.4.

The size, aspect ratio, and density of carbides are lowest at a tempering temperature of 200 °C due to the formation of eta (η) transitional carbides of iron, or η -Fe₂C, which has an orthorhombic crystal structure, as previously described.^[18,30,31] At tempering temperatures of 350 °C and higher, these carbides transform into Fe₃C, resulting in an increase in their size. Additionally, new, finer carbides appear at 500 °C and above, which contribute to secondary hardening. These carbides are likely to be the carbides and carbonitrides of elements such as Cr, Mo, and V that are present in the steel composition.^[13]

3.6. Matrix Analysis by EBSD

The area fractions of various grain boundaries in the samples are plotted against tempering temperature in Figure 16. The grain boundaries have been divided into low, medium, and high angle grain boundaries with misorientation angles of 2–5°, 5–15°, and >15° respectively. As can be observed, the fractions of these various boundaries did not change significantly with tempering from the DQ state, even up to the tempering temperature of 700 °C. The high angle boundaries are around 60%, whereas low and medium angle boundaries constitute about 40% together, indicating the presence of significant amount of sub-boundaries in the matrices of the samples.

Similar to the grain boundaries, the Kernel average misorientation (KAM) and the density of the GND, shown in Figure 17 and 18 respectively, also do not show any change from the DQ state through the tempering at various temperatures up to 700 °C. The density of GND in most of the areas of the matrices appears to be between 3 and $4 \times 10^{15} \text{ m}^{-2}$, although some areas have lower density (the blue areas of the images in Figure 18). The KAM values in the specimens are mostly in the range of 1–2°

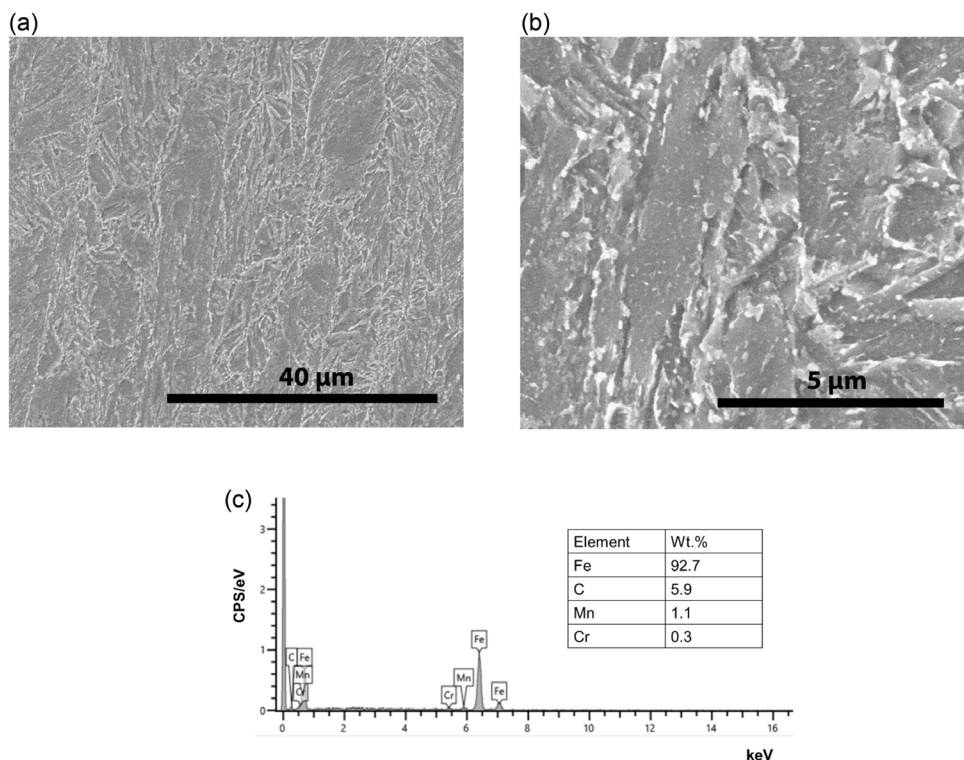


Figure 13. SEM micrographs of the steel after tempering at 700 °C at a) low (3000X) and b) high (20,000X) magnifications and c) typical EDX spectra of precipitates.

(green–blue areas in the images of Figure 17) with small amount of very low ($<1^\circ$) KAM areas (blue areas of the images in Figure 17). Thus, since a low local misorientation in the matrix indicate a low density of GND and vice versa, the KAM and density of GND in the matrices of the specimens corroborate each other.

The grain orientation spread (GOS) images of the specimens are shown in **Figure 19**. The GOS of all the tempered specimens as well of the DQ state are mostly high (3–5°), indicating a higher amount internal misorientation and thus higher degree of deformation or strain within the grain. This suggests that the matrices have high dislocation density with no recrystallized feature. This points to the absence of ferrite in the matrices of all the specimens, even after tempering at 700 °C. In addition, it is to be noted that no RA was detected from EBSD phase analysis confirming the finding from the XRD experiments (Figure 4).

The misorientation angle distributions (MAD) of the matrix of the samples subjected to the EBSD investigation are plotted in **Figure 20** comparing it with that of the theoretical distribution of randomly oriented structure. It can be observed that all the specimens (the DQ as well as the tempered conditions) showed a MAD which significantly deviates from the theoretical MAD for recrystallized ferrite. All the studied conditions showed peaks of MAD at $\approx 5^\circ$, 54° , and 60° . As reported by Gorgues et al.,^[35] the peaks at 60° may correspond to martensite or lower bainite, at 54° to upper bainite and at 5° to lower or upper bainite. Thus, the current EBSD results indicate that the matrices of the specimens

consist of a mixture of martensite and bainite. It is apparent that the steel in its DQ condition had a martensite and bainite as matrix, and the matrix phases became tempered at different temperatures up to 700 °C, but ferrite did not form.

The SEM images presented in Figure 8–13 indicate that it is challenging to differentiate between bainite and tempered martensite. However, the distribution of carbides within the laths and along the boundaries resembles bainitic microstructures. Despite this resemblance, these microstructures are often reported as tempered martensite in the literature.^[18] The presence of bainite, as identified in this study by EBSD experiments, opens new avenues for research in characterizing quenched and tempered (Q&T) structural steels. The goal is to distinguish between bainite and tempered martensite and evaluate their effects on mechanical properties, which will be explored in future studies.

According to Morito et al.^[36,37] the fractions of special boundaries or block boundaries for a martensitic matrix in Fe–C as well as in alloy steels are observed to be highest at the $60^\circ/[011]$ combination of the misorientation angle and rotation axis. Smaller fractions may also be observed at $60^\circ/[111]$, $49.5^\circ/[011]$, and $10.5^\circ/[011]$. The special boundaries at $60^\circ/[111]$ may also indicate the presence of another low temperature phase, i.e., bainite. The special boundary fractions of the specimens determined from EBSD are presented in **Table 2**. These results confirm that the matrices of the specimens contain martensitic and bainitic phases, as was found from the MAD results in Figure 20, and they do not change significantly with tempering in all cases.

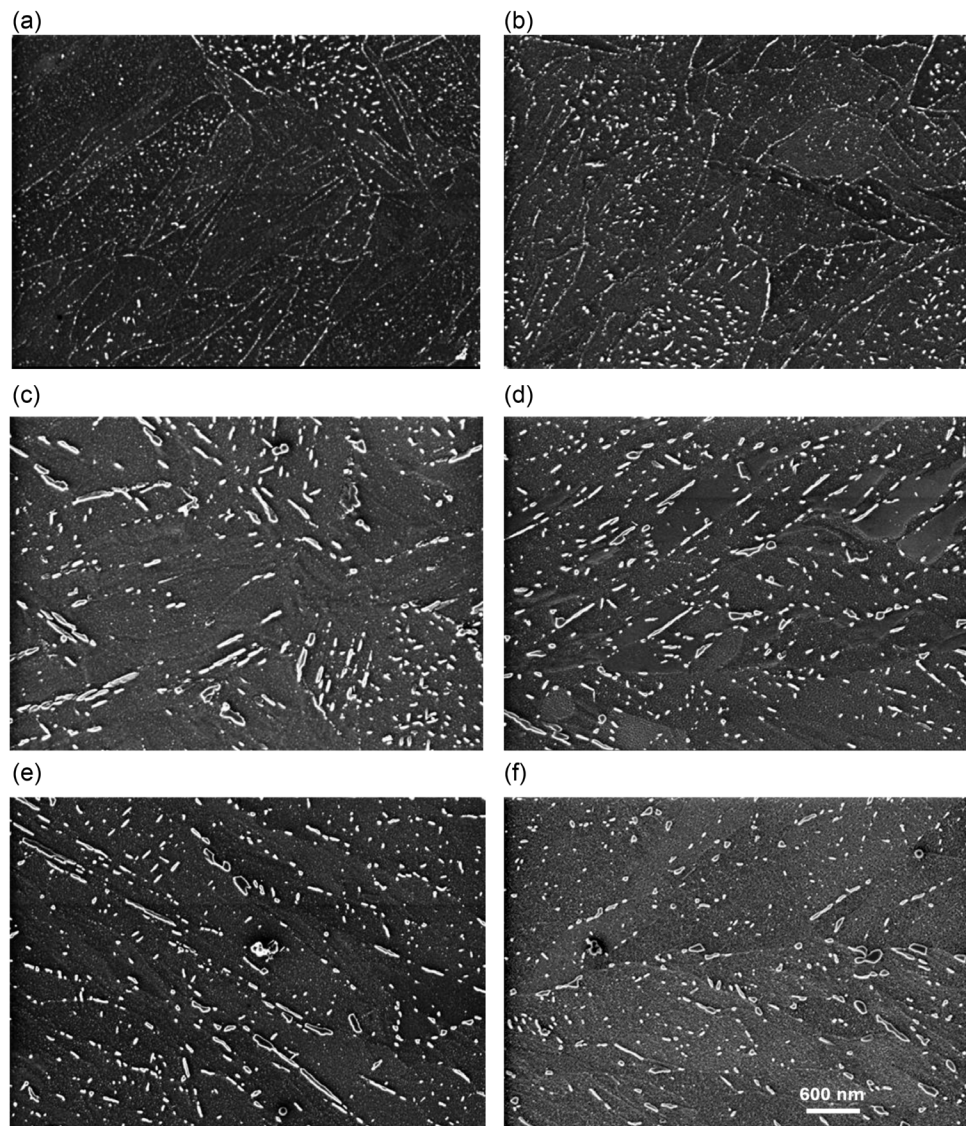


Figure 14. SEM micrographs showing distribution of carbides in the steel after a) DQ, b) 200 °C tempering, c) 350 °C tempering, d) 500 °C tempering, e) 550 °C tempering, and f) 700 °C tempering.

4. Discussion

4.1. Structural Changes During Tempering Stages

This study revealed that the hardness of the S1300-type steel investigated in this study decreased as the tempering temperature increased (Figure 1). This change occurred in three stages of tempering due to some specific microstructural and crystallographic changes in the steel. The microstructure of the steel remained martensitic from its DQ state to all the tempered states up to 700 °C, as shown in Figure 8–13. The c/a ratio, as shown in Figure 4, also confirms that the crystal remained BCT throughout from its DQ state to its tempered state up to 700 °C. This is contrary to the common belief that lath martensite transforms into ferrite and spheroidized cementite when tempered above 400 °C.^[25] The reason for the stabilization of the lath martensite

microstructure in all the tempering states of the current steel is presumably the presence of boron in the steel composition. Boron is known to increase hardenability and enables the martensite to remain stable even at high tempering temperatures. This is facilitated by the fact that boron tends to segregate at the austenite grain boundary, delaying the nucleation of ferrite.^[12]

The EBSD study revealed that the microstructures included bainite, which coexisted with tempered martensite under all the tempering conditions examined. However, as mentioned earlier, further investigations are needed to differentiate bainite from tempered martensite in the microstructures, particularly since the formation of bainite in such structural grades Q&T steels has not been previously reported.^[18]

The variation in hardness in Figure 1 was influenced by the presence of lath martensite during all three tempering stages.

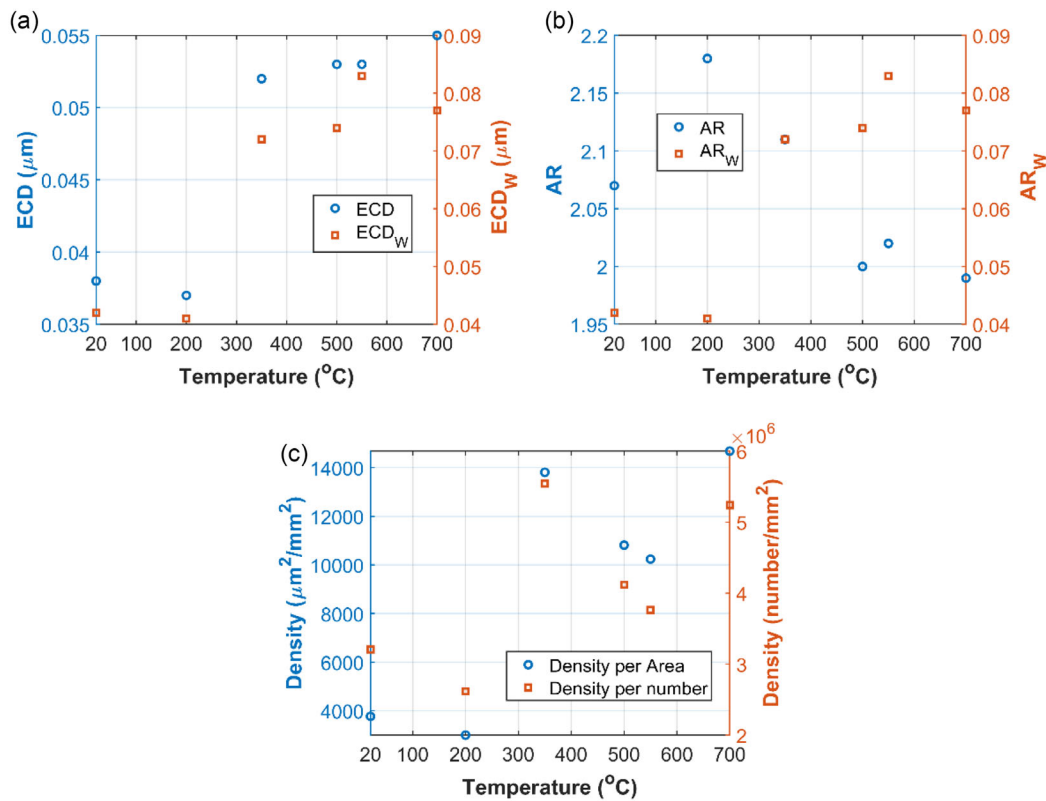


Figure 15. Carbide distribution parameters of the specimens against tempering temperature: a) equivalent circle diameter (ECD) and weighted average of ECD with area as the weighting factor (ECD_w), b) aspect ratio (AR) and weighted aspect ratio (AR_w), and c) area density and number density.

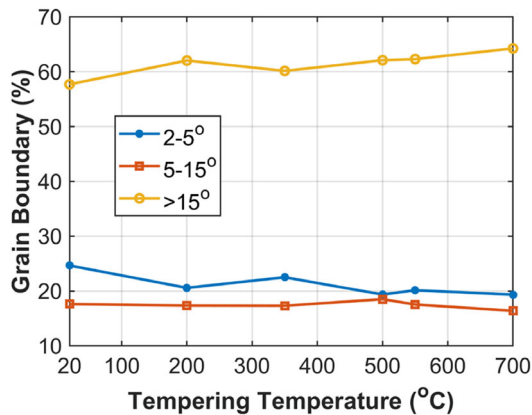


Figure 16. Area fractions of grain boundaries with various misorientation angles in the steel matrix as a function of tempering temperature.

Additionally, hardness was influenced by the coarsening of martensite grains and the nucleation and growth of different types of precipitates that are visible in the microstructures in Figure 8–13. These factors were discussed in detail in the results sections.

Furthermore, some interesting crystallographic changes were noticed during tempering stage 1 and stage 3 in contrast to tempering stage 2. As expected, the calculated FWHM, c/a ratio, and microstrain drastically reduced with the tempering temperature during tempering stage 2, but the change was relatively very slow

(and even almost negligible at some temperatures) during tempering stage 2 and 3 (see Figure 5–7). The calculated crystallite size values, on the contrary, increased with tempering temperature during stage 2 but showed similarly slower change during stages 2 and 3. These can be explained based on the microstructural changes observed at different tempering temperatures, in Figure 8–13.

During stage 1 of tempering, the precipitation of fine coherent $\eta\text{-Fe}_2\text{C}$, in their abundance on the intralath and lath-boundary, strengthened the crystals, but the strengthening effect is nullified by the softening effect of tempering process. As a result, the calculated microstrain values after tempering at 200 °C remained almost unchanged compared to its initial DQ state, as shown in Figure 7. Previous studies on high-strength steels suggest that, in some cases, a reasonable increase in hardness and tensile properties can be expected during stage 2 tempering compared to their quenched state.^[18] This might explain why the measured FWHM values remained almost unchanged, and the c/a ratio marginally increased at a tempering temperature of 200 °C, as illustrated in Figure 5 and 6. On the other hand, the change in crystallite size in tempering stage 1, in Figure 7, was influenced by the grain boundary pinning effect of $\eta\text{-Fe}_2\text{C}$ precipitates, which restricted martensite crystallite growth. Hence, the calculated crystallite size remained unchanged during tempering stage 1. In addition, any undissolved alloying element during austenitizing treatment, such as Mo, Cr, and Nb, may also be responsible for restricting martensite grain growth.^[33,34]

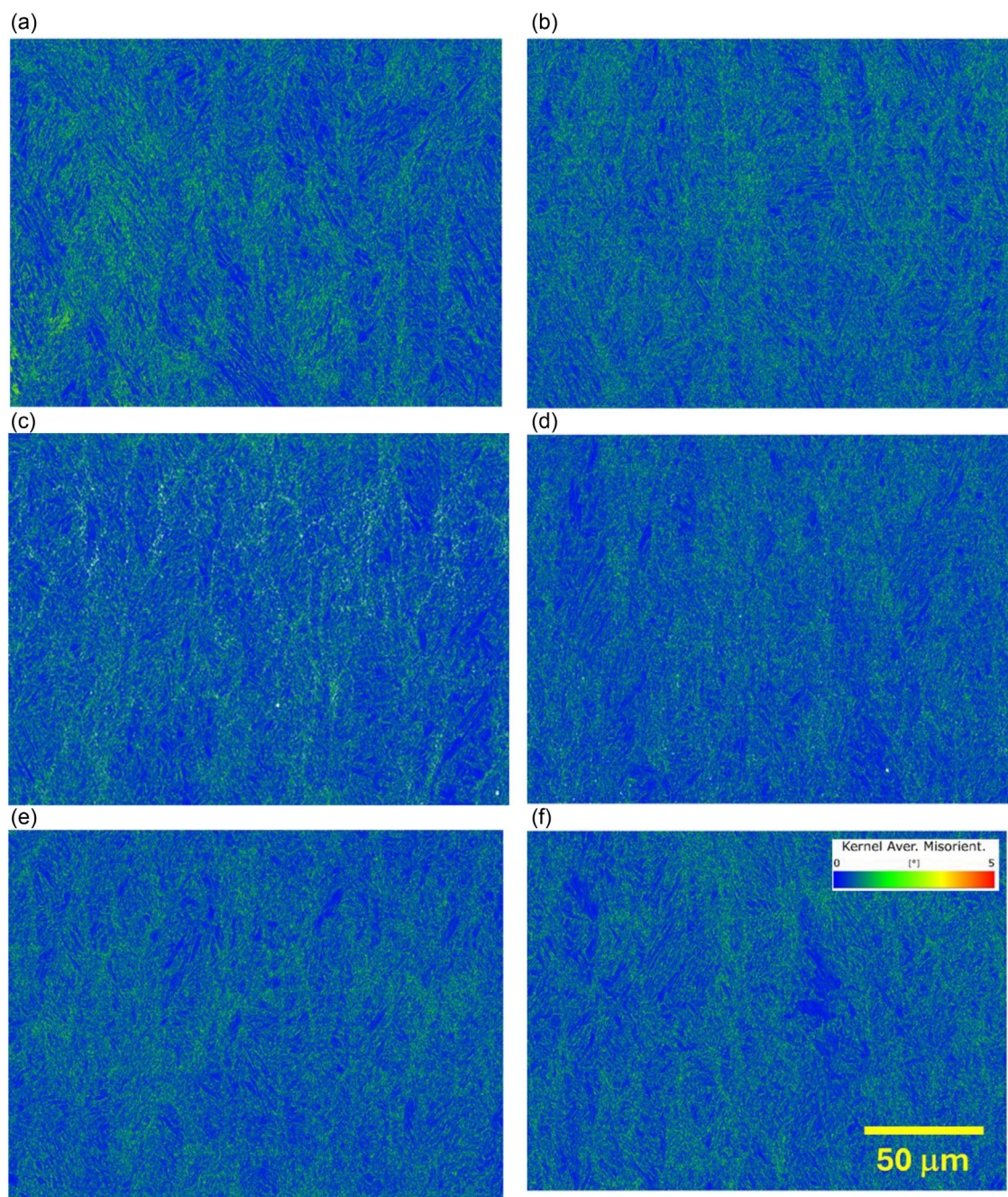


Figure 17. KAM of the steel after a) DQ, b) 200 °C tempering, c) 350 °C tempering, d) 500 °C tempering, e) 550 °C tempering, and f) 700 °C tempering.

During tempering stage 3, the calculated c/a ratio, FWHM and microstrain values again were relatively less dependent on tempering temperature compared to their trends observed in stage 2, as shown in Figure 5–7. This change was mainly due to secondary hardening that commenced just after the tempering temperature of 500 °C and peaked at 550 °C. During the secondary hardening stage, the newly formed fine carbides and carbonitride precipitates of V, Mo, and Cr were responsible for introducing additional microstrain in the martensite crystal, which was not completely nullified by the softening effect of HTT at stage 3.

As a result, the calculated microstrain, c/a ratios, and FWHM values were found to be less sensitive to tempering temperatures at stage 3. With regard to the trend in crystallite size observed in stage 3, the newly formed fine precipitates, responsible for secondary hardening, were responsible for limiting crystal growth. Hence, the crystallite size also remained less sensitive to the tempering effect during stage 3.

An interesting observation from the trend observed in microstrain and crystallite size values in tempering stage 3, as shown in Figure 7, is that the secondary hardening was operative

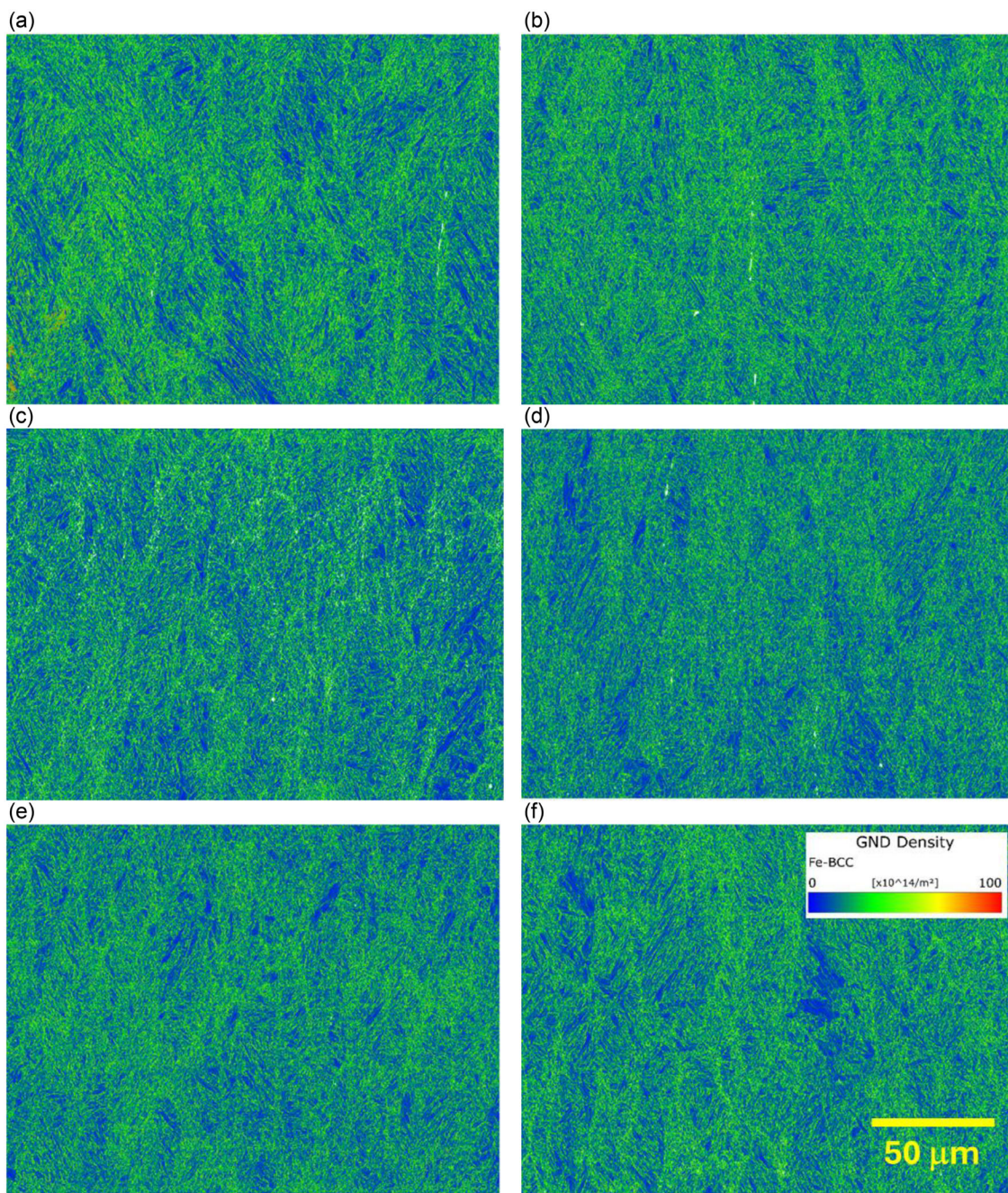


Figure 18. GND of the steel after a) DQ b) 200 °C tempering, c) 350 °C tempering, d) 500 °C tempering, e) 550 °C tempering, and f) 700 °C tempering.

throughout tempering stage 3. This can be explained based on the following two possible mechanisms: (1) new fine precipitates responsible for secondary hardening were continuously formed throughout tempering stage 3, and/or (2) the precipitates responsible for secondary hardening were only formed at a tempering temperature of around 550 °C (where a secondary hardening peak was observed) and had limited growth throughout tempering stage 3. Evidence of fine precipitates was observed in the microstructure of the steel at the intralath

location throughout tempering stage 3 (see Figure 12 and 13). The exact chemistry and the growth kinetics of these precipitates in this new ultrahigh-strength structural steel warrant further study.

The carbide analysis in Figure 14 and 15 reveals the size distribution and density of the precipitates under the different tempering conditions examined. However, the exact chemistry of the precipitates was not identified, and this remains a limitation of this study.

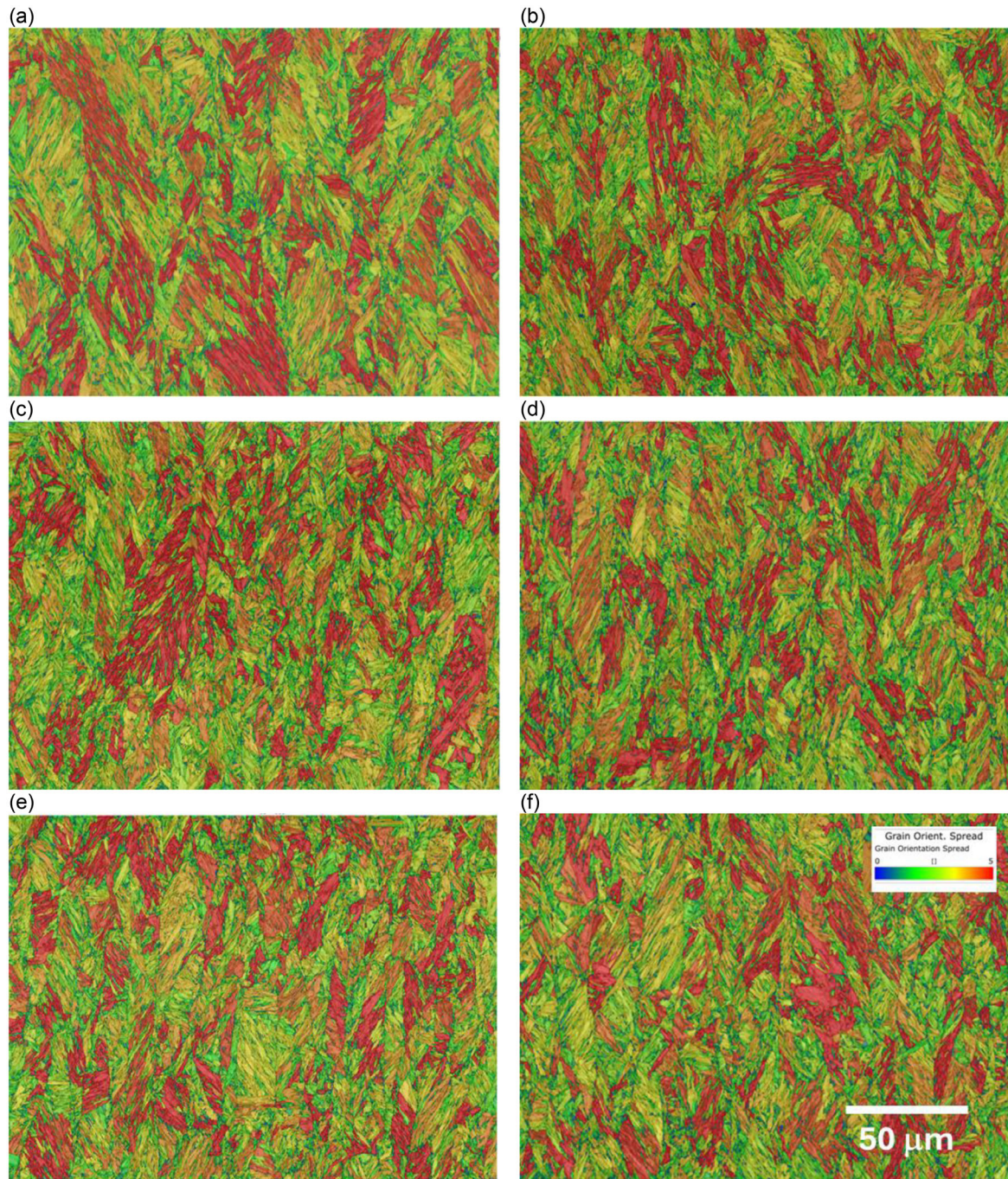


Figure 19. GOS of the steel after a) DQ, b) 200 °C tempering, c) 350 °C tempering, d) 500 °C tempering, e) 550 °C tempering, and f) 700 °C tempering.

4.2. New Empirical Relationships

An attempt was made to establish an empirical relationship between the measured hardness and some of the measured crystallography parameters of the UHSS studied. A strong linear correlation of the hardness of the steel in its DQ and tempered states (Figure 1) with the FWHM data was found as shown in **Figure 21a**. The relation between these two parameters can be expressed by the following empirical equation:

$$H_T = a \times \text{FWHM} + b \quad (2)$$

where H_T is the Vickers hardness number of the steel at individual DQ and tempered condition, FWHM is the average values of the FWHM determined for various diffraction angles (in degree) as shown in Figure 6, and a and b are material constants, which can be calculated from the gradient and Y-intersection of the best-fit line. $a = 176.9$ and $b = 259.8$ were found for the steel under the heat treatment conditions studied. Previous studies

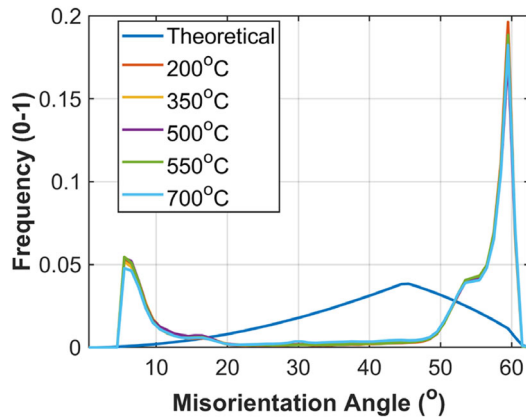


Figure 20. MAD of the steel matrix in DQ and various tempered conditions in comparison with theoretical distribution.

Table 2. Special boundary areas of the steel matrix as determined from EBSD in DQ and various tempering conditions from this study.

Specimen	Boundary area fraction [%] of different angle/rotation axis pairs			
	60°/[011]	60°/[111]	49.5°/[011]	10.5°/[011]
DQ	28.4	13.6	3.6	13.6
200 °C tempering	26.1	16.6	3.7	13.6
350 °C tempering	25.6	13.9	3.2	13.7
500 °C tempering	25.6	12.5	3.1	14.1
550 °C tempering	26.2	14.8	3.4	13.6
700 °C tempering	25.3	13.9	3.5	12.8

by other researchers also reported a strong correlation between hardness and FWHM for various steel grades.^[38]

In addition, a new parameter from the measured microstrain and crystallite size was found to have an even better linear correlation with the observed change in hardness of the UHSS, as illustrated in Figure 21b. The relationship is shown in Equation (3).

$$\Delta H = c \times \text{MSP} + d \quad (3)$$

where c and d are material constants, which can be calculated from the gradient and Y-intercept of the best-fit line. For the steel at the heat treatment conditions, $a = 0.37$, and $b = 4.04$. ΔH is the change in hardness (in percentage), which was calculated using Equation (4), as shown in the following:

$$\Delta H = \frac{H_{\text{DQ}} - H_{\text{T}}}{H_{\text{DQ}}} \times 100 \quad (4)$$

where H_{DQ} is the hardness of DQ steel, and H_{T} is the hardness at a tempering temperature (both in Vickers hardness number).

In Equation (3), MSP is a new dimensionless number, proposed here as a “microstrain-crystallite size parameter,” which was calculated using Equation (5), as shown in the following

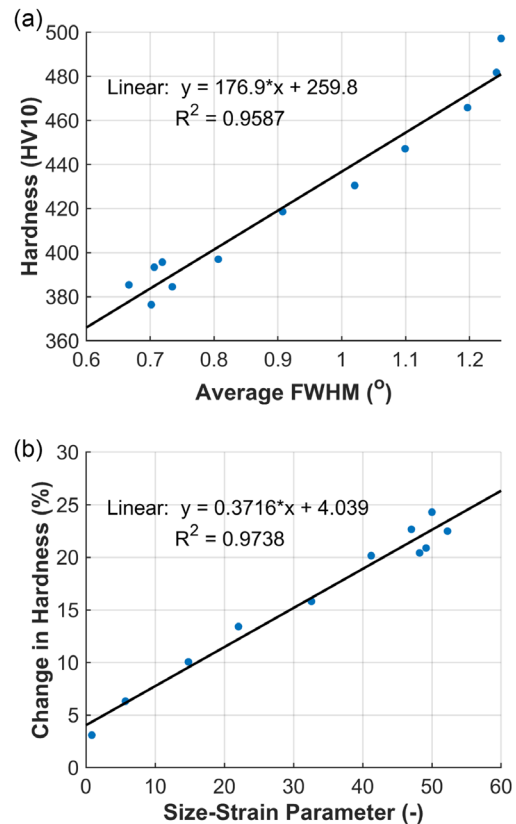


Figure 21. a) Hardness vs. average FWHM showing a linear relationship and b) change in hardness with tempering plotted against the newly proposed size-strain-parameter, showing a linear relationship.

$$\text{MSP} = \left(\frac{M_{\text{DQ}} - M_{\text{T}}}{M_{\text{DQ}}} \times 100 \right) + \ln \left(\frac{S_{\text{DQ}} - S_{\text{T}}}{S_{\text{DQ}}} \times 100 \right) \quad (5)$$

where M_{DQ} is the measured microstrain at DQ state, M_{T} is the measured microstrain at a tempering temperature, S_{DQ} is the measured crystallite size at DQ state (nm), and S_{T} is the measured crystallite size at a tempering temperature. Thus, MSP is a dimensionless number, proposed here as a “microstrain-crystallite size parameter.”

The relationship between hardness, microstrain, and crystallite size in Equation (3) has not been reported previously and is proposed by the authors of this article. This equation will be valuable for predicting hardness for different steel grades that undergo tempering and will also be beneficial for industrial steel product development trials.

4.3. Comparison with Other Structural and UHSS

As previously mentioned, UHSS developed for the automotive and aerospace industries often utilize significantly different alloy compositions (typically containing high levels of silicon and/or manganese) as well as distinct processing methods, such as TRIP or quenching and partitioning (Q&P).^[8–16] Consequently, the microstructures of these UHSS primarily exhibit a bainitic/martensitic

structure and contain a notably high amount of RA. This is in stark contrast to the microstructure of the S1300 type steel reported here, which is predominantly martensitic and free of RA. Furthermore, those mentioned UHSS are significantly expensive due to the requirement of high alloy content and complex processing routes, and they are not suitable for developing structural steel grades.

When comparing the S1300 type steel investigated here with other high-strength structural steel grades such as S960 and S1100, it was found that most published literature on structural steels, including S900 and S1100, has primarily focused on the microstructure–property relationship in welded joints rather than on alloy design and heat treatment for product development, which is the aim of this study for S1300 type steels.^[1–3,18] Consequently, this study offers a detailed theoretical foundation for steel industries looking to develop products for high or ultrahigh-strength structural steel grades. Despite certain limitations, the microstructures observed in S1300 and S1100 are comparable to those of the S1300 steel examined in this study. However, two clear distinctions were noted. First, the S1300-type steel did not contain any RA, which is commonly found in other structural steel grades. Second, it features a combination of bainite and tempered martensite, a pairing that has not been documented in other structural steel grades.

4.4. Industrial Outlook from the Work

This study investigated a boron-containing low-carbon alloy steel, similar to S1300, developed via direct-quench and tempered (DQ&T) product development routes. The study included a detailed characterization of the steel grade under varied tempering temperatures, and the measured hardness (and predicted YS values from previously published equations) values indicated that the grade specification (i.e., YS of 1300 MPa) can be met when the DQ state is tempered for 2 h within the stage 1 that ranges up to 200 °C. However, tempering to a higher temperature, up to 700 °C, was not a complete waste of effort. Rather, it revealed that the hardness range achievable from its DQ state to tempering up to 700 °C ranged from 497 HV10 to 376 HV10. These hardness values are expected to meet YS specifications of other structural grades with lower YS, such as S900 to S1100, which are also the grades of high demand by the lifting and excavating market sector. In addition, the study provided an opportunity for an improved, thorough understanding of the effect of DQ&T on a steel composition similar to S1300, aiding suitable alloy design and process optimization for future S1300 grade developments.

5. Conclusions

This study investigated the effect of DQ and 2 h tempering heat treatments on the hardness, microstructure, and relevant crystallographic parameters of a new generation ultrahigh-strength S1300-type structural steel. The conclusions are as follows. 1) Tempering of martensite in the steel occurs in three distinct stages. At low temperatures (stage 1), the hardness remained almost unchanged. During medium-temperature tempering (stage 2), it decreased significantly with temperature. Finally, at higher temperatures (stage 3), it again showed relatively low

sensitivity to tempering temperatures. 2) The mechanisms of the 3 stages of tempering of martensite were identified based on the measured microstructural and crystallographic changes. The microstructure of the steel remained martensitic from its DQ state to all the tempered states up to 700 °C. The microstructures were free from ferrite formation at all the tempering temperatures studied, and further EBSD analysis confirmed this finding. Coexistence of bainite with tempered martensite was identified in EBSD analysis, which was, however, not easy to distinguish under high-resolution SEM images. The fine precipitate of η -Fe₂C that nucleated during tempering stage 1 was responsible for maintaining the strength. However, the strength decreased significantly in tempering stage 2 due to the formation and growth of Fe₃C and other alloy precipitates. In stage 3, secondary hardening once again enhanced the strength of the material. Variation in FWHM, c/a ratio, microstrain, and crystallite size with tempering temperature also showed 3 distinct trends contributing to the observed hardness changes. 3) The steel exhibited no RA in its DQ and tempered states, contrary to the widespread reporting of RA in ultrahigh-strength structural steels. 4) A strong linear correlation between hardness, FWHM, and a new parameter based on microstrain and crystallite size of martensite was empirically derived and proposed.

Appendix

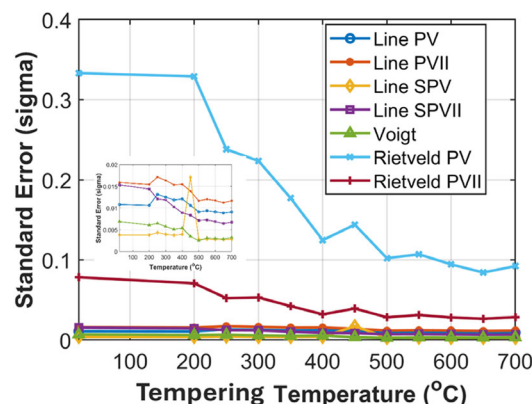


Figure A1. The average standard error for all XRD peaks versus tempering temperatures. The results indicate that the Voigt peak function fitting method exhibited the lowest error compared to other techniques implemented using TOPAS software. These other methods included Rietveld refinement methods (Pseudo-Voigt (PV), Pearson VII (PVII)) and line fitting methods (Pseudo-Voigt (PV), Pearson VII (PVII), Split Pseudo-Voigt (SPV), and Split Pearson VII (SPVII)).

Acknowledgements

The authors wish to thank Mr. Alun Davies and Dr. Francis Sweeney from Sheffield Hallam University and Mr. Sabri Sengo and Ms. Monika Krugla from Tata Steel Netherlands for their lab technical support during this study.

Conflict of Interest

The authors declare no conflict of interest.

Data Availability Statement

The data that support the findings of this study are available from the corresponding author upon reasonable request.

Keywords

hardness, lattice strains, low carbon martensite, microstructures, quenching and tempering, ultrahigh-strength steels

Received: December 26, 2024

Revised: June 16, 2025

Published online:

- [1] M. Tümer, C. Schneider-Bröskamp, N. Enzinger, *J. Manuf. Process.* **2022**, 82, 203.
- [2] X. Qiang, X. Jiang, F. S. K. Bijlaard, H. Kolstein, *Eng. Struct.* **2016**, 112, 60.
- [3] W. Guo, D. Crowther, J. A. Francis, A. Thompson, Z. Liu, L. Li, *Mater. Des.* **2015**, 85, 53.
- [4] S. Das, A. Karmakar, S. B. Singh, in *High-Performance Ferrous Alloys* (Ed: R. Rana), Springer International Publishing, Cham **2021**, pp. 83–112.
- [5] Y. Tian, J. Zhang, Z. Wang, Z. Y. Shi, X. Li, M. C. Zhao, *Steel Res. Int.* **2024**, 95, 2300290.
- [6] J. Zhang, M. C. Zhao, Y. Tian, J. Zhang, Z. Wang, Y. C. Zhao, L. Peng, *Materials* **2024**, 17, 1636.
- [7] J. Tomków, M. Landowski, D. Fydrych, G. Rogalski, *Marine Struct.* **2022**, 81, 103120.
- [8] *Automotive Steels: Design, Metallurgy, Processing and Applications* (Eds: R. Rana, S. B. Singh), Cambridge, Elsevier (Woodhead imprint), UK **2016**.
- [9] R. Rana, E. Cordova-Tapia, L. Morales Rivas, C. Garcia-Mateo, *Mater. Sci. Forum* **2023**, 1105, 219.
- [10] R. Rana, S. Chen, A. Haldar, S. Das, *Arch. Metall. Mater.* **2017**, 62, 2331.
- [11] R. Rana, E. Cordova-Tapia, J. A. Jimenez, L. Morales-Rivas, C. Garcia-Mateo, *Philos. Mag. Lett.* **2024**, 104, 2322552.
- [12] H. Chen, L. Zhao, S. Lu, Z. Lin, T. Wen, Z. Chen, *Metals* **2022**, 12, 2184.
- [13] J. Li, D. Zhan, Z. Jiang, H. Zhang, Y. Yang, Y. Zhang, *J. Mater. Res. Technol.* **2023**, 23, 172.
- [14] S. Singh, T. Nanda, *Int. J. Sci. Res. Develop.* **2014**, 2, 2321.
- [15] B. D. Jana, A. K. Chakrabarti, K. K. Ray, *Mater. Sci. Technol.* **2003**, 19, 80.
- [16] R. Rana, E. Cordova-Tapia, L. Morales-Rivas, J. A. Jimenez, C. Garcia-Mateo, *Mater. Sci. Eng.: A* **2025**, 931, 148236.
- [17] B. Santillana, R. Rana, A. Burghardt, *IOP Conf. Ser. Mater. Sci. Eng.* **2023**, 1274, 012027.
- [18] G. Krauss, *Steel Res. Int.* **2017**, 88, 1700038.
- [19] B. Hutchinson, D. Lindell, M. Barnett, *ISIJ Int.* **2015**, 55, 1114.
- [20] T. A. Kop, J. Sietsma, S. Van Der Zwaag, *J. Mater. Sci.* **2001**, 36, 519.
- [21] Q. Gao, C. Wang, F. Qu, Y. Wang, Z. Qiao, *J. Alloys Compd.* **2014**, 610, 322.
- [22] C. Liu, M. Huang, Q. Ren, Y. Ren, L. Zhang, *Steel Res. Int.* **2022**, 93, 2200044.
- [23] S. Afkhami, T. Björk, J. Larkiola, *J. Constr. Steel Res.* **2019**, 158, 86.
- [24] A. Navarro-López, J. Sietsma, M. J. Santofimia, *Metall. Mater. Trans. A Phys. Metall. Mater. Sci.* **2016**, 47, 1028.
- [25] H. Bhadeshia, R. Honeycombe, *Steels: Microstructure and Properties*, Butterworth-Heinemann **2017**.
- [26] P. Scardi, M. Leoni, R. Delhez, *J. Appl. Crystallogr.* **2004**, 37, 381.
- [27] G. Kimmel, D. Day, G. A. Frank, A. Landau, *X-ray Diffraction (XRD) Characterization of Microstrain in and Uranium Alloys X-ray Diffraction (XRD) Characterization of Microstrain in Some Iron and Uranium Alloys*, Annual Report of International Atomic Energy Commission **1996**, pp. 28–56.
- [28] J. He, J. Ye, E. J. Lavernia, D. Matejczyk, C. Bampton, J. M. Schoenung, *J. Mater. Sci.* **2004**, 23, 6957.
- [29] H. Kitahara, R. Ueji, N. Tsuji, Y. Minamino, *Acta Mater.* **2006**, 54, 1279.
- [30] R. Mishnev, Y. Borisova, T. Kniazuk, S. Gaidar, R. Kaibyshev, *Metals* **2023**, 13, 1399.
- [31] Y. Hirotsu, S. Nagakura, *Trans. Japan Inst. Met.* **1974**, 15, 129.
- [32] Y. Hirotsu, S. Naqakijras, *Acta Metall.* **1972**, 20, 645.
- [33] V. Dudko, D. Yuzbekova, S. Gaidar, S. Vetrova, R. Kaibyshev, *Metals* **2022**, 12, 2177.
- [34] W.-S. Lee, T.-T. Su, *J. Mater. Process. Technol.* **1999**, 87, 198.
- [35] A.-F. Gourgues, H. M. Flower, T. C. Lindley, *Mater. Sci. Technol.* **2000**, 16, 26.
- [36] S. Morito, H. Tanaka, R. Konishi, T. Furuhashi, T. Maki, *Acta Mater.* **2003**, 51, 1789.
- [37] S. Morito, X. Huang, T. Furuhashi, T. Maki, N. Hansen, *Acta Mater.* **2006**, 54, 5323.
- [38] P. Fu, C. R. hu, Z. Xu, G. Ding, C. Jiang, *Appl. Surf. Sci.* **2018**, 431, 165.